Environ Earth Sci (2010) 61:1215–1225
DOI 10.1007/s12665-009-0445-2

ORIGINAL ARTICLE

The impacts of hysteresis on variably saturated hydrologic response and slope failure

Brian A. Ebel · Keith Loague · Ronaldo I. Borja

Received: 9 April 2009 / Accepted: 29 December 2009 / Published online: 14 April 2010

Abstract This investigation employs 3D, variably saturated subsurface flow simulation to examine hysteretic effects upon the hydrologic response used to drive unsaturated slope stability assessments at the Coos Bay 1 (CB1) experimental catchment in the Oregon Coast Range, USA. Slope stability is evaluated using the relatively simple infinite slope model for unsaturated soils driven by simulated pore-water pressures for an intense storm that triggered a slope failure at CB1 on 18 November 1996. Simulations employing both hysteretic and non-hysteretic soil–water retention curves indicate that using either the drying soil–water retention curve or an intermediate soil–water retention curve that attempts to average the wetting and drying retention curves underestimates the near-surface hydrologic response and subsequently the potential for slope failure. If hysteresis cannot be considered in the hydrologic simulation, the wetting soil–water retention curve, which is seldom measured, should be used for more physically based slope stability assessment. Without considering hysteresis or using the wetting soil–water retention curve, the potential for landsliding in unsaturated materials may be underestimated and a slope failure could occur when simulations predict stability.

Keywords Hysteresis · InHM · Landslide · Unsaturated · Modeling · Hillslope

Abbreviations

CB1	Coos Bay 1
InHM	Integrated hydrology model
FS	Factor of safety
1D	One-dimensional
2D	Two-dimensional
3D	Three-dimensional
USA	United States of America

Introduction

Slope failures continue to be one of the most deadly and destructive natural hazards in the United States, causing between 25 and 50 fatalities and approximately $3.5 billion in property damage annually (U.S. Geological Survey 2004). Landslides and debris flows can also load sediment to fluvial systems, degrading aquatic habitat (e.g., Lamberti et al. 1991; Gomi et al. 2002). The potential causes of slope failures include the influences of hydrology, geology, soils, volcanoes, seismicity, and land-use practices (Sidle and Ochiai 2006). Hydrologic events serve as the most frequent trigger of landslides in many regions throughout the world (Van Asch et al. 1999; U.S. Geological Survey 2004). The growing field of hydrogeomorphology recognizes the importance of hydrologic response in governing many geomorphic

B. A. Ebel (✉) · K. Loague
Department of Geological and Environmental Sciences, Stanford University, Stanford, CA 94305-2115, USA
e-mail: bebel@usgs.gov

R. I. Borja
Department of Civil and Environmental Engineering, Stanford University, Stanford, CA 94305-4020, USA

Present Address:
B. A. Ebel
U.S. Geological Survey, Menlo Park, CA 94025-3561, USA

processes, including slope failure (Scheidegger 1972; Dunne 1990, 1994; Sidle and Onda 2004).

The current conceptual understanding of rainfall-induced landslides relies principally on the reduction of effective stress via positive pore-water pressure development (Terzaghi 1943). Recent research has demonstrated that a reduction in capillary stress from a loss of matric suction can also trigger shallow slope failure (e.g., Rahardjo et al. 1994; Fourie et al. 1999; Likos and Lu 2004; Godt et al. 2009). Whether it is the loss of suction or positive pore-water pressures that reduce shear strength, it is clear that unsaturated zone hydrology is a driving force behind the timing and location of slope failure initiation. Hysteresis in the nonlinear soil–water retention curve, referring to different relationships between pressure head and soil–water content depending on whether the soil is wetting or drying, can strongly affect the movement of water in the unsaturated zone, yet is seldom incorporated into hydrologic models.

Selected modeling efforts that examine variably saturated fluid flow and slope failure at both catchment and watershed scales are summarized in Table 1. While the studies mentioned in Table 1 have contributed much understanding, only the study presented here conducts 3D unsaturated flow simulation, including hysteretic flow processes, coupled to slope stability assessment. The well-studied Coos Bay 1 (CB1) experimental catchment is the field site used to investigate the effects of hysteresis in simulating hydrologic response to rainfall that triggers unsaturated slope failure. A large storm in November 1996 that caused slope failure at CB1 provides both the motivation and the parameterization data for this work. The inclusion of hysteresis allows for comparison between simulations using the wetting, drying, and mean (i.e., intermediate between the wetting and drying) soil–water retention curves to hysteretic results. The hydrologic model employed here is the integrated hydrology model (InHM); the slope stability assessment is conducted using the infinite slope approach. This study builds upon prior hydrologic-response simulations at the CB1 field site (see Ebel et al. 2007b, 2008; Ebel and Loague 2008). The intention of this study is not to exactly replicate the slope failure mechanisms at CB1, which are likely triggered by bedrock fracture flow (Montgomery et al. 2002, 2009). Instead, the principal objective here is to investigate the impacts of hysteresis upon near-surface hydrologic response and unsaturated slope stability for a Coos-Bay-like location in the presence of hysteresis in the soil–water retention curve. The presence of sandy soils at CB1 (see Torres et al. 1998), coupled with relatively permeable bedrock and reduced root strength from timber harvest (Schmidt et al. 2001), provides the ingredients for potential unsaturated slope failure (see Lu and Godt 2008) at a CB1-like location. The testing of the hysteretic parameterization for controlled sprinkling experiments, including comparison against pressure head and soil–water content data, presented in Ebel et al. (2007b) provides a firm foundation for the work presented here.

The Coos Bay 1 experimental catchment study site

The CB1 field site, which consists of a small (860 m^2) unchanneled valley on the Oregon coast in the USA, is shown in Fig. 1. Maximum elevations at the ridgeline shown in Fig. 1 are 300 m above sea level. The site is small enough to facilitate detailed characterization and monitoring of hydrologic response. Topography for CB1 was generated from a detailed theodolite survey at approximately 1 m^2 horizontal grid scale (Montgomery et al. 1997). CB1 has a north-facing aspect, an average slope of 43°, and receives approximately 1,600 mm of rainfall [based on 29 years of data from the nearby North Bend, Oregon airport (Taylor et al. 2005)]. Timber harvest occurred in 1987, followed by

Table 1 Selected process-based simulation efforts that have considered both variably saturated hydrologic response and slope stability

Reference	Hydrologic response		Slope stability dimensionality
	Dimensionality	Hysteresis	
Anderson and Howes (1985)	1D	No	1D
Anderson et al. (1988)	2D	No	2D
Ng and Shi (1998a, b)	2D	No	2D
Hattendorf et al. (1999)	3D[a]	No	2D
Gasmo et al. (2000)	2D	No	2D
Iverson (2000)	1D	No	1D
Cho and Lee (2002)	2D	No	2D
Tsaparas et al. (2002)	2D	No	2D
Wilkinson et al. (2002)	3D[b]	No	2D
Mirus et al. (2007)	3D	No	1D
Simoni et al. (2008)	3D	No	1D
This study	3D	Yes	1D

[a] 1D unsaturated flow coupled to 3D saturated flow

[b] Quasi-3D

herbicide application (Roundup®) in 1988 (Torres 1997), and planting of Douglas Fir (*Pseudotsuga menziesii*) seedlings in 1989 (Montgomery et al. 1997). Vegetation after reforesting consisted primarily of Alder (*Alnus*), Douglas Fir (*Pseudotsuga menziesii*), sword fern (*Polystichum munitum*), and bramble (*Rubus*). A high intensity storm in November 1996 that resulted in six landslide-related fatalities in the Oregon Coast Range (Roering et al. 2003) triggered a slope failure at CB1 (Montgomery et al. 2009). The failure mass, representing removal of approximately 180 m^3 of material from CB1, travelled nearly 1 km downslope as a debris flow (Montgomery et al. 2009). A long-term research effort at CB1 conducted site characterization and hydrologic observations from artificial sprinkling and natural storms (see Anderson et al. 1997a, b; Montgomery et al. 1997, 2002; Torres et al. 1998; Montgomery and Dietrich 2002; Ebel et al. 2007a). The observations and measurements facilitated hydrologic-response simulation of the 3 week-long sprinkling experiments (Ebel et al. 2007b) and natural storms (i.e., continuous simulation from 1990 to 1996; see Ebel et al. 2008). A system of wooden platforms (see Fig. 1) facilitated instrument installation and monitoring with minimum impact to the CB1 surface and subsurface.

Analysis of the CB1 observations and hydrologic-response simulations show that (1) subsurface storm flow is the primary runoff generation mechanism (Montgomery et al. 1997, 2002; Ebel et al. 2007b); (2) flow through fractures in the shallow, weathered bedrock exerts the most significant control on pore-water pressure development in the CB1 soil (Anderson et al. 1997b; Montgomery et al. 1997, 2002); (3) unsaturated flow provides an additional control on the timing of pore-water pressure and runoff development (Torres et al. 1998; Montgomery et al. 2002; Ebel et al. 2007b); and (4) incorporating the geometry and hydraulic properties of subsurface permeability contrasts is important for accurate simulation of hydrologic response (Ebel et al. 2007b, 2008). It should be noted that the simulations reported here are different from the event-based simulations of the three CB1 sprinkling experiments (see Ebel et al. 2007b) in that the storm simulated in this effort is natural (i.e., not irrigated with sprinklers) and has a much larger rainfall intensity magnitude (i.e., causing slope failure).

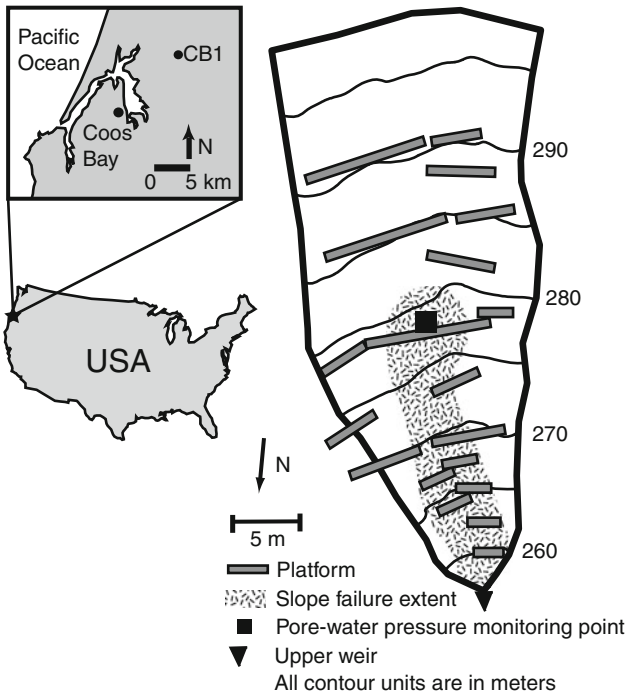

Fig. 1 Map showing the location of CB1 in coastal Oregon, USA and a diagram of the CB1 topography, instrumentation platforms, approximate observed slope failure extent in 1996, and simulated pore-water pressure monitoring point. Note that the topography was surveyed before the failure and does not reflect the post-failure topography

Methods

Hydrologic response simulation: the integrated hydrology model (InHM)

The hydrologic-response model InHM (VanderKwaak 1999) quantitatively estimates 3D unsaturated flow in porous media and macropores and 2D surface flow employing the finite-element method. InHM has been successfully employed to simulate hydrologic response for a variety of hydrologic environments (see VanderKwaak 1999; VanderKwaak and Loague 2001; Loague and VanderKwaak 2004; Loague et al. 2005, 2006; Ebel and Loague 2006, 2008; Jones et al. 2006; Ran et al. 2007; Heppner et al. 2006, 2007; Smerdon et al. 2007; Heppner and Loague 2008; Mirus et al. 2007, 2009; Ebel et al. 2009).

InHM estimates subsurface flow using:

$$\nabla \cdot f^{a}\vec{q} \pm q^{b} \pm q^{e} = f^{v}\frac{\partial \varphi S_{w}}{\partial t} \quad (1)$$

where f^{a} is the area fraction associated with each continuum [–], $\vec{q}$ is the Darcy flux [L T^{-1}], q^{b} is a specified rate source/sink [T^{-1}], q^{e} is the rate of water exchange between the subsurface and surface continua [T^{-1}], f^{v} is the volume fraction associated with each continuum [–], φ is porosity [L^{3} L^{-3}], S_{w} is water saturation [L^{3} L^{-3}], and t is time [T]. The Darcy–Buckingham flux is:

$$\vec{q} = -k_{rw}\frac{\rho_{w} g}{\mu_{w}}\vec{k}\nabla(\psi + z) \quad (2)$$

where k_{rw} is the relative permeability [–], ρ_{w} is the density of water [M L^{-3}], g is the gravitational acceleration

[L T^{-2}], μ_w is the dynamic viscosity of water [M L^{-1} T^{-1}], $\vec{k}$ is the permeability vector [L^2], z is the elevation head [L], and ψ is the pressure head [L]. The diffusion wave approximation to the depth-integrated shallow water equations is employed to estimate the transient surface water flow, with the conservation of water on the land surface expressed by:

$$\nabla \cdot \psi_s^{\text{mobile}} \vec{q}_s \pm a_s q^b \pm a_s q^e = \frac{\partial \left(S_{w_s} h_s + \psi_s^{\text{store}} \right)}{\partial t} \quad (3)$$

where ψ_s is water depth [L], $\vec{q}_s$is the surface water velocity [L T^{-1}], a_s is the surface coupling length scale [L], q^b is the source/sink rate (i.e., rainfall/evaporation) [T^{-1}], q^e is the surface–subsurface water exchange rate [T^{-1}], and h_s is the average height of non-discretized surface microtopography [L]; the superscripts mobile and store refer to water exceeding and held in depression storage, respectively (VanderKwaak 1999). The first-order coupling (see VanderKwaak 1999; Ebel et al. 2009) between the surface and subsurface continua occurs via a thin soil layer of thickness, a_s in Eq. 3. Surface water velocities are calculated utilizing a two-dimensional form of the Manning's equation calculated as:

$$\vec{q}_s = -\frac{\left(\psi_s^{\text{mobile}} \right)^{2/3}}{\vec{n} \Phi^{1/2}} \nabla (\psi_s + z) \quad (4)$$

where $\vec{n}$ is the Manning's surface roughness tensor [T $L^{-1/3}$] and Φ is the friction (or energy) slope [–]. A more detailed description of InHM can be found in VanderKwaak (1999).

Adaptive time-steps (Δt) are used to decrease simulation run time. The finite-element mesh used in the InHM simulations to represent CB1 is the same as used by Ebel et al. (2007b, 2008), consisting of 264,220 prism elements (138,544 nodes) in the subsurface and 4,804 triangular elements (2,474 nodes) for the surface. Vertical discretization (Δz) is variable from 0.04 m in the near surface to 1.67 m near the base of the finite element mesh. Horizontal discretization (Δx, Δy) is also variable from 0.4 m in areas of interest to 2.0 m near the upgradient boundaries.

Slope stability estimation: the infinite slope model

Assuming a continuous phase of pore-air pressure, u_a[$ML^{-1}T^{-2}$], equal to the atmospheric pressure (i.e., zero for gage pressure), the infinite slope equation provides an expression for the factor of safety (FS) [–] given by:

$$\text{FS} = \frac{(C' + \Delta C) + (\gamma_t z_{uz} \cos^2 \alpha - S\, u_w) \tan \varphi'}{\gamma_t z_{uz} \sin \alpha \cos \alpha} \quad (5)$$

where C' is the effective soil cohesion [$ML^{-1}T^{-2}$], ΔC is the root cohesion [$ML^{-1}T^{-2}$], γ_t is the total unit weight of the soil [$ML^{-2}T^{-2}$], z_{uz} is the thickness of unsaturated soil [L], α is the slope angle [°], S is the saturation [L^3 L^{-3}], u_w is the pore-water pressure [$ML^{-1}T^{-2}$], and φ' is the angle of internal friction [°]. The saturation is estimated as the soil–water content, θ [L^3 L^{-3}], normalized by porosity, n [L^3 L^{-3}]. The formulation of Eq. 5 relies on the effective stress framework initially proposed by Schrefler (1984), which replaces the Bishop (1959) parameter, χ [–], with saturation. Borja (2006) explains the thermodynamic basis for the aforementioned effective stress framework. It should be noted that the infinite slope equation given here is slightly different that that proposed by Lu and Godt (2008), which uses the effective saturation rather than saturation (see Lu and Likos 2006).

Boundary-value problems

Hydrologic response boundary-value problem

Hydrologic parameterization

The fence diagram in Fig. 2 shows the hydrogeologic units used to parameterize the CB1 boundary-value problem. The CB1 subsurface parameterization used in this study is based on prior analysis by Ebel et al. (2007a, b, 2008) employing the extensive information from the field site (see Montgomery et al. 1997; Torres et al. 1998; Anderson and Dietrich 2001; Anderson et al. 2002). Ordinary Kriging of 630 measured soil and saprolite depths (Montgomery et al. 1997; Schmidt 1999) in and surrounding CB1 provide a detailed characterization of the near-surface geology to generate the soil and saprolite hydrogeologic unit geometries shown in Fig. 2. The weathered bedrock layer shown in Fig. 2 is 4 m thick at the ridgecrest and thins downslope (Anderson 1995; Anderson et al. 2002; Montgomery et al. 2002), pinching out at the downgradient boundary. The lowermost layer in Fig. 2 is the bedrock. The porosity value for the soil of 0.5 m^3 m^{-3} is taken as the soil–water content value at saturation (Torres et al. 1998; Montgomery et al. 2002). Porosity values for the saprolite (i.e., 0.15 m^3 m^{-3}), weathered bedrock (i.e., 0.15 m^3 m^{-3}), and bedrock (i.e., 0.12 m^3 m^{-3}) come from the deep drill core taken at the ridge crest (Anderson et al. 2002).

Figure 3 shows the measured hysteretic soil–water retention data (see Torres et al. 1998) and the estimated wetting, drying, and mean non-hysteretic soil–water retention curves generated using the van Genuchten (1980) method. Hysteresis in the InHM characterization of soil–water retention was represented using the approach described by Scott et al. (1983) and Kool and Parker (1987) to scale scanning curves between the wetting and drying soil–water retention curves and was tested at CB1 by Ebel et al. (2007b). The saprolite, weathered bedrock, and

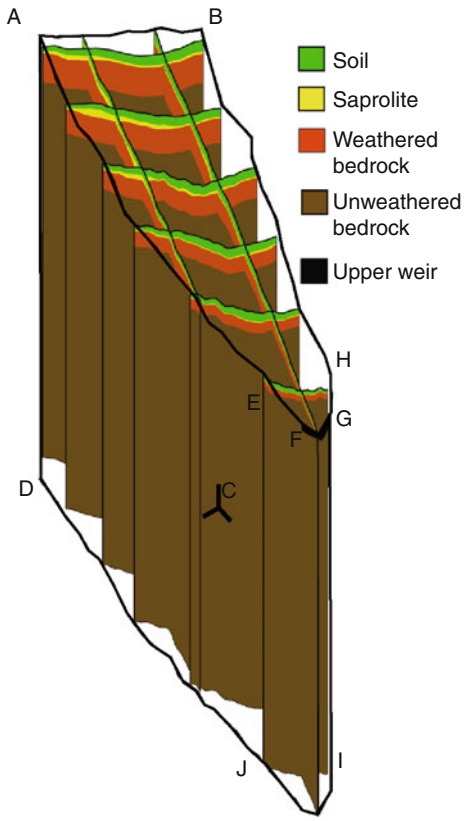

Fig. 2 Fence diagram illustrating the hydrogeologic characterization of the CB1 boundary-value problem with letters used to describe the boundary conditions (after Ebel et al. 2008)

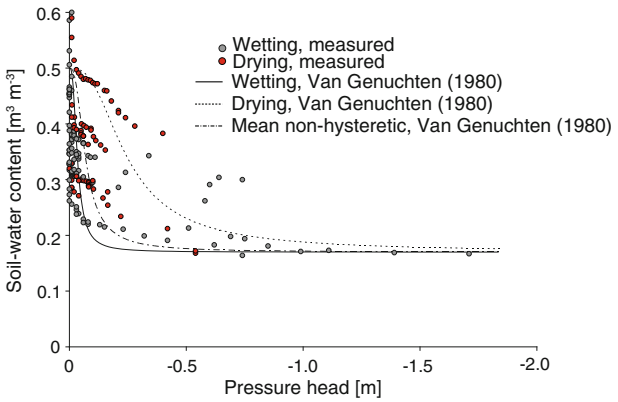

Fig. 3 Observed soil–water retention data (after Torres et al. 1998) and the estimated wetting, drying, and mean (i.e. intermediate between the wetting and drying) non-hysteretic soil–water retention curve approximated using the van Genuchten (1980) method (after Ebel et al. 2007b)

unweathered bedrock are parameterized using non-hysteretic characteristic curve values from Wu et al. (1999) and the van Genuchten (1980) method. Unsaturated hydraulic conductivity functions are estimated from the van Genuchten (1980) parameters for each respective layer. The saturated hydraulic conductivity values are 3.4×10^{-4} m s^{-1} for the soil, 2.0×10^{-5} m s^{-1} for the saprolite, 1.7×10^{-5} m s^{-1} for the weathered bedrock, and 5.0×10^{-7} m s^{-1} for the bedrock. These saturated hydraulic conductivity values are based on evaluation of piezometer slug tests for the soil, saprolite, and weathered bedrock (Ebel et al. 2007a, 2008) and calibration for the bedrock (Ebel et al. 2008).

Hydrologic boundary conditions

The InHM boundary conditions are shown in Fig. 2, which identifies the boundary condition endpoints referenced by capital letters in this section. No flow boundary conditions are specified for the drainage divides at the side boundaries for the surface (AEF and BHG) and subsurface (ADJE and BCIH), the upgradient surface drainage divide (AB) at the ridge crest, and the basal subsurface boundary condition (DCIJ). The CB1 upper weir [metal sheeting sealed to bedrock with roofing tar (Montgomery et al. 2009)] is represented using an impermeable subsurface boundary condition (along FG from the surface to the top of the weathered bedrock) and a critical depth (see Chow 1959; Freeze 1978) surface flow boundary condition (FG). The upgradient (ABCD) and downgradient (EHIJ) subsurface boundary conditions (except for the upper weir) use a local head boundary condition. The local head boundary condition represents a known, temporally variable hydraulic head value at a point outside the boundaries of the finite-element mesh (see Heppner et al. 2007; Ebel et al. 2007b, 2008) to calculate the volumetric boundary flux, $Q_{b,l}$ [L^3 T^{-1}] at each boundary node using:

$$Q_{b,l} = k_{rw}\frac{\rho_w g}{\mu_w}\vec{k}A\frac{h_l - h_{b,pm}}{dl} \quad (6)$$

where h_l is the total head at the local head point [L], $h_{b,\,pm}$ is the total head for the porous medium equation at the boundary node [L], A is the nodal area [L^2], and dl is the (positive) distance in the x–y plane between the node and the regional sink point [L]. The local head point is treated as a vertical line of constant potential below the specified local head point, which results from using the two-dimensional distance (dl) in Eq. 6.

The upgradient local head (ABCD) is parameterized using the level of the deep well at the CB1 ridge crest (see Ebel et al. 2008). The downgradient local head point used for all the simulations is a location of consistent observed surface saturation in the channel downslope of CB1 just below the lower weir. The mean rainfall rate from three onsite-automated raingages is used to parameterize the specified flux for the surface boundary condition (ABHGFE in Fig. 2). Rainfall is assumed to be spatially uniform across the relatively small CB1 catchment, which is consistent with the Coefficient of Uniformity (see Christiansen, 1942) of 90% estimated by Ebel et al. (2007a).

The temporal resolution of the rain gages is 600 s. Figure 4 shows the hyetograph and cumulative rainfall (see Montgomery et al. 2009) used during the simulations reported here, up to the time of observed slope failure. The peak rainfall rate of near 40 mm h^{-1} presumed to trigger slope failure at CB1 is approximately an order of magnitude larger than typical peak rainfall rates observed at the site during nearly 7 years of observation (see Ebel et al. 2008).

Hydrologic initial conditions

The hydrologic response initial conditions consist of pressure head at every subsurface node and the water depth at every surface node. These initial conditions are generated using InHM simulations, self-consistent for each soil–water retention curve scenario (i.e., wetting, drying, mean, and hysteretic), to drain CB1 from near saturation to an approximate observed water table location based on observations from a deep well and piezometers. The InHM simulations for assessing the failure conditions begin on 15 November 1996 at midnight, which facilitates "spinning up" the subsurface, via simulation, preceding the most intense portion of the storm that triggered the CB1 slope failure. The relatively short duration spinup period prevents pumping effects in the Kool and Parker (1987) hysteresis method.

Slope stability boundary-value problem

Slope stability parameterization

The simulated pore-water pressures from the hydrologic-response simulations are used to drive the unsaturated slope stability estimation. If estimation of slope stability at locations between finite-element nodes using simulated pore-water pressures is needed, the protocol of Krahn et al. (1996) could be employed. The root cohesion, ΔC, contributes to the mobilized shear strength in Eq. 5 as a surface force on the base of the soil mass and therefore must use the basal rather than lateral root cohesion. Measurements made at CB1 after the slope failure (Montgomery et al. 2009), following the protocol of Schmidt et al. (2001), provide the parameterization of the infinite-slope model used in this study, which are C'_{soil} of 0.9 kPa, $\Delta C_{root\text{-}basal}$ of 0.1 kPa, γ_t of 15.7 kN m^{-3}, $\varphi'$of 40°, α of 43°, and a locally variable z_{uz} that accounts for the soil depth at the InHM finite-element node at the failure plane. Figure 1 shows the simulated monitoring location where failure is assessed, the location of which was chosen to reflect the most likely location of failure initiation based on observations (Montgomery et al. 2009). The observed basal failure surface was nearly planar and parallel to the ground surface (Montgomery et al. 2009), consistent with the failure surface assumptions of Eq. 5.

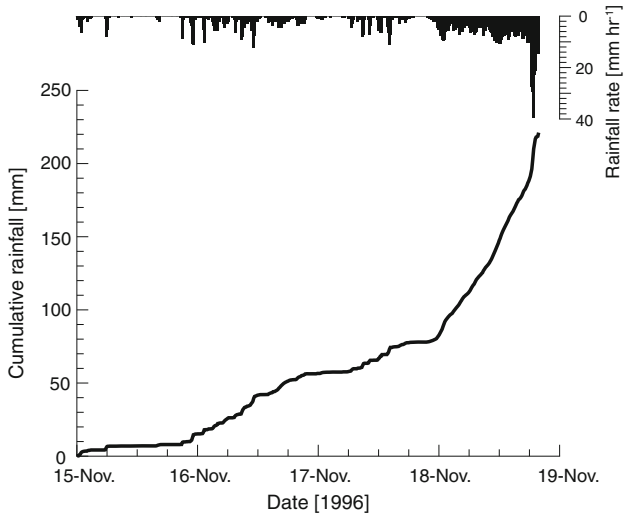

Fig. 4 Hyetograph and cumulative rainfall at CB1 during the simulation period

Results

Simulated hydrologic response

Integrated hydrologic response

Figure 5 shows the observed upper weir discharge and the simulated hydrographs for the wetting, drying, mean, and hysteretic soil–water retention curves. The observed discharge shows a slow rise between 16 November to 18 November in response to intermittent rainfall of moderate intensities. Beginning 18 November, the observed discharge begins to rise rapidly in response to near-continuous rainfall, peaking slightly before the timing of observed failure following a spike increase of rainfall rate to near 40 mm h^{-1}. The observed discharge ceases at the time of slope failure, when the weir is destroyed by the sliding regolith. Relative to the observed discharge, all the simulated discharges are underestimated at small discharges between 15 November to 18 November. For all four soil–water retention curves, the discharge is well simulated for the first 16 h of 18 November. The simulated discharges for all four soil–water retention curve scenarios are relatively close in magnitude to the observed discharge at the time of failure. In Fig. 5, the simulated discharges continue for the period after failure, showing the continued rise in discharge in response to the 40 mm h^{-1} rainfall pulse that triggers failure followed by rapid drainage of the subsurface (as indicated by the simulated discharge) for 1 day following failure. Other than the slightly better simulation of discharge by the hysteretic soil–water retention curve in

the period from 16 November to 18 November, the four soil–water retention curves produced nearly identical discharges, in large part because the bedrock saturated hydraulic conductivity places a predominant control on simulated discharge (Ebel et al. 2008) at CB1. While the simulated discharges suggest that the hydrologic response is simulated reasonably accurately at CB1 for the storm causing slope failure, the discharge represents the integrated hydrologic response and may not reveal differences in response at distributed locations throughout the site which may be important for slope failure initiation.

Distributed hydrologic response

Figure 6a shows simulated saturation snapshots at the soil–saprolite interface at the time of the observed slope failure, which is similar in spatial patterns for all four soil–water retention curve scenarios because saturation development at the soil–saprolite interface is predominantly controlled by convergent interface topography. Owing to the *n* parameter in the van Genuchten (1980) relationships being constant across all four scenarios (see Scott et al. 1983; Kool and Parker 1987), the unsaturated hydraulic conductivity functions are the same and so the magnitudes of simulated saturations in Fig. 6a are similar. Figure 6b shows simulated pore-water pressure snapshots at same time and locations as Fig. 6a. The pore-water pressure development is also largely controlled by subsurface interface topography. The effect of the characteristic curves for the soil layer can be seen by comparing the mean, drying, wetting, and hysteretic scenarios. For example, the drying scenario in Fig. 6b has lower simulated pore-water pressures because for a given saturation, the pressure heads are smaller (i.e., more negative) on the drying soil–water retention curve compared to on the wetting curve (see Fig. 3). Consistent with the simulated saturation results, the wetting scenario has the highest simulated pore-water pressures and the drying scenario has the lowest simulated pore-water pressures of the four scenarios presented here. Unfortunately, there are no unsaturated zone observations available to evaluate the simulated unsaturated zone response at CB1 during the failure storm.

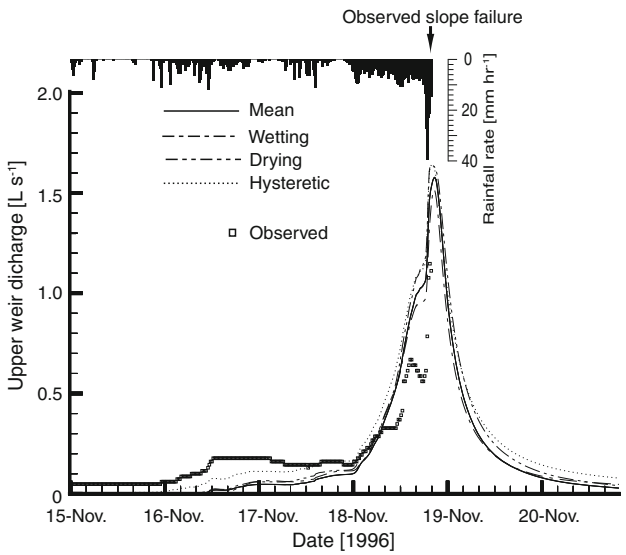

Fig. 5 Observed and selected simulated upper weir hydrographs (note that the observed record ends at the time of slope failure initiation). The hyetograph generating the observed and simulated runoff is shown up to the point of failure initiation

Slope stability assessment

Figure 7a shows a time series of FS values calculated using Eq. 5 for the simulated monitoring point (see Fig. 1) for the mean retention curve scenario. The minimum simulated FS value approaches 1.0 (i.e., failure) approximately one and a half hours after the observed slope failure time, but the FS in Fig. 7a never dips below 1.0. Figure 7b shows the FS values for the mean, drying, wetting, and hysteretic scenarios. The drying scenario is the most stable, the wetting scenario is the least stable (although the hysteretic scenario is approximately equivalent to the wetting scenario), and the mean scenario is in the middle. The hysteretic scenario values are similar to the drying FS values at the initiation of the storm and quickly approach the wetting scenario FS values. Based on the FS results shown here, the wetting soil–water retention curve provides the most conservative estimate of hydrologically driven slope failure (i.e., most failure prone) and the mean scenario is like an ensemble of the drying and wetting simulations. Use of the wetting soil–water retention curve is physically consistent with extreme rainfall events likely to trigger slope failure, which should converge quickly from a hysteretic scanning curve to the primary wetting curve with thorough soil wetting. It is clear from the FS estimates in Fig. 7b that the drying soil–water retention curve, which is the most easily measured in the laboratory and the most frequently used by hydrologists and geotechnical engineers, will overestimate FS values in hysteretic soils like those at CB1.

Discussion

As noted previously, while the FS values shown in Fig. 7a approach 1.0, the FS estimates never fall below 1.0 (i.e., no slope failure). Previous CB1 hydrologic-response simulation efforts (see Ebel et al. 2007b, 2008) indicated that the missing fracture flow processes, which could not be adequately simulated using an effective saturated hydraulic conductivity approach, prevented representing the pore-water

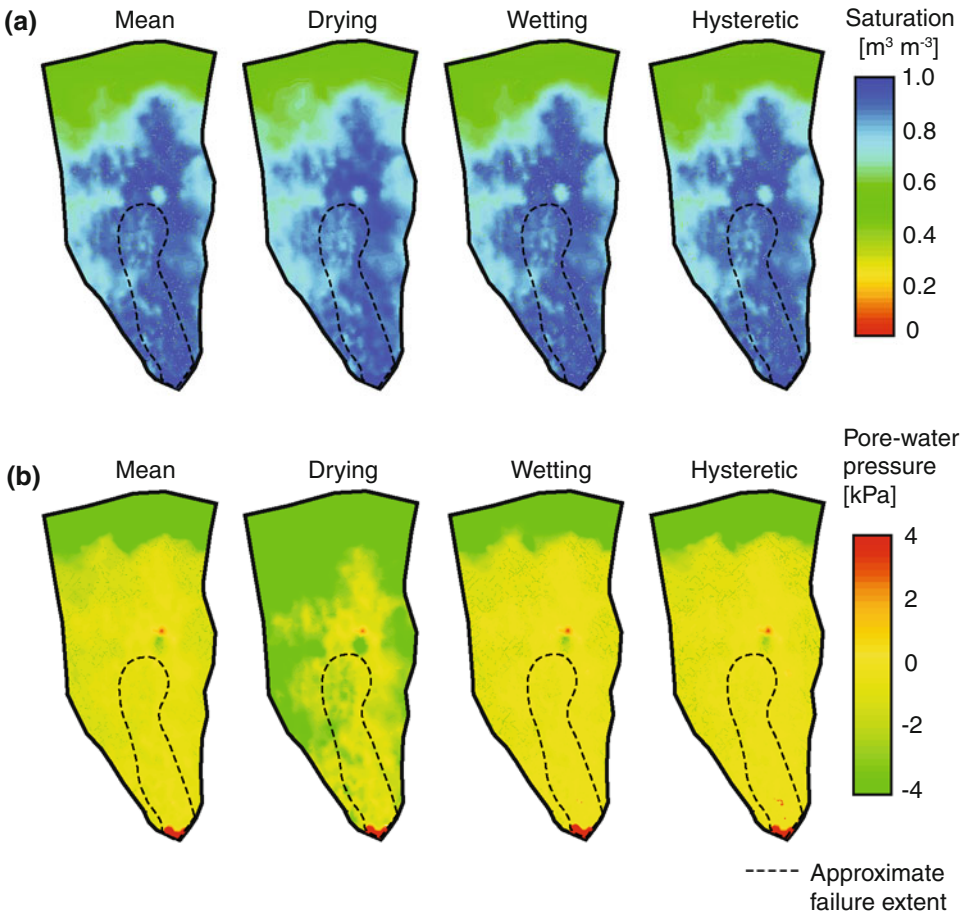

Fig. 6 **a** Simulated saturation snapshots at the soil-saprolite interface for the mean, drying, wetting, and hysteretic soil–water retention curve scenarios at the observed time of the 1996 slope failure initiation. **b** Simulated pore water pressure snapshots at the soil-saprolite interface for the mean, drying, wetting, and hysteretic soil–water retention curve scenarios at the observed time of the 1996 slope failure initiation

pressure hotspots observed in the field data (see Montgomery et al. 1997, 2002, 2009). Our results suggest that the rainfall drives the slope to near-failure by reducing the stability contribution of negative pore-water pressures; at the CB1 site, this is insufficient to induce failure but instead poises the slope for failure like a "loaded gun" until localized failure is triggered by positive pore-water pressures resulting from exfiltrating fracture-flow (Montgomery et al. 2009). This points to the difficulty in simulating hydrologically driven slope failure in locations like CB1 since it is nearly impossible to know the fracture locations a priori (Montgomery et al. 2002, 2009). While not all sites are fracture flow dominated, factors such as lithology (e.g., Evans 1982; Andronopoulos 1982; Roering et al. 2005), saturated hydraulic conductivity heterogeneity (e.g., Wilson and Dietrich 1987; Johnson and Sitar 1990; Vieira and Fernandes 2004), and unsaturated zone response (Fourie et al. 1999; Godt et al. 2009) have been demonstrated to affect landsliding. The aforementioned complexities will confound simple (e.g., steady-state, reduced dimensionality, non-distributed) hydrologic simulation approaches. Obviously, the same complexities, when not well represented (e.g., the fracture flow component in the study reported here), can pose problems for more rigorous hydrologic approaches as well. However, physics-based hydrologic-response models have the potential to represent fracture flow, lithologic heterogeneity, saturated hydraulic conductivity variations, and unsaturated zone physics if sufficient parameterization data are available.

The slope stability estimation approach used here is not without its limitations (see Wright et al. 1973); the physical rigor of the hydrologic-response model far exceeds that of the slope stability assessment in this study. The limit equilibrium method used here (a) assumes that peak strength is mobilized simultaneously along the failure surface (Duncan 1996), (b) presumes force inclinations can be specified a priori (Duncan 1996), (c) allows only for rigid body displacements to occur (Wong 1984), and (d) overestimates failure potential because it does not include 3D effects (lateral forces) (Stark and Eid 1998). Perhaps the most significant challenge in slope failure estimation is to correctly incorporate the contributions of spatially variable root strength that provides stability on the periphery of a landslide; these root effects are known to be important at CB1 (Schmidt et al. 2001) and cannot be included in Eq. 5 in a physically correct form. The inclusion of root strength into unsaturated slope stability assessments in a physically meaningful way may represent a significant

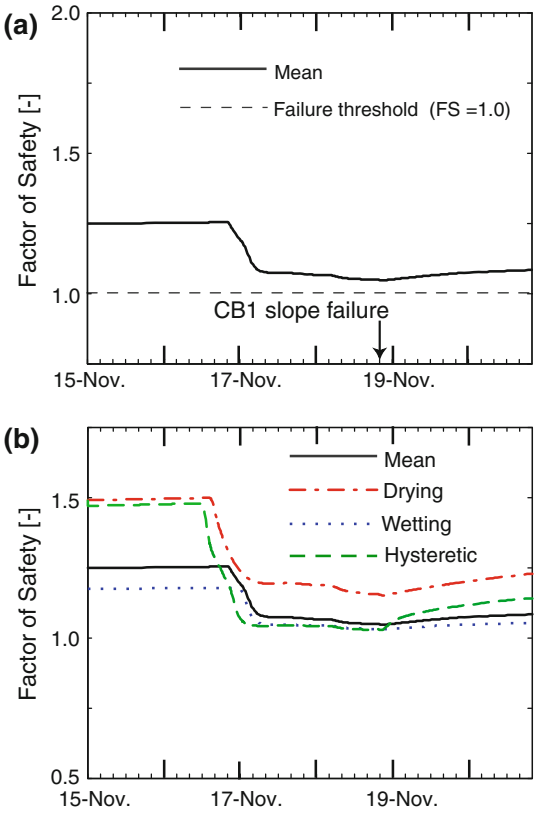

Fig. 7 Time series of the factor of safety (FS) values from the infinite slope stability assessment. **a** For the mean soil–water retention curve scenario at the simulated observation point (see Fig. 1). The *dashed line* at FS equal to 1.0 indicates incipient slope failure, values of FS below 1.0 are typically assumed to have failed. **b** For the mean, drying, wetting, and hysteretic soil–water retention curve scenarios at the simulated observation point

advance in our ability to estimate slope failure initiation. It is worth pointing out that while more sophisticated slope stability estimation methods exist, such as the finite-element method (e.g., Griffiths and Lane 1999), it is critical to understand the complex hydrology triggering failure, including hysteresis, before moving onto a fully coupled, fully 3D analysis. Despite the drawbacks of the infinite slope approach, the method can still provide insight into the complex interplay of the factors that trigger slope failure, as shown here.

One of the original objectives of the long-term and controlled sprinkling efforts at CB1 was to first understand the hydrology and then use a high intensity sprinkling experiment to cause a landslide at the site (WE Dietrich, personal communication 1988). The intention was to use sophisticated hydrologic and geotechnical measurements to monitor hydrologically driven landslide initiation at the field scale at CB1. Sprinkling experiments, such as the one envisioned at CB1, that induce slope failure in a controlled, highly monitored setting at the field scale are needed to advance the development and testing of hydrologically driven slope failure models.

Summary

Comparisons of simulated saturation and pore-water pressures show the sensitivity of saturation and pore-water pressures to the soil–water retention curves. The FS values from hysteretic and non-hysteretic simulations show that wetting retention curve scenario is the most failure prone while the drying retention curve scenario is the least failure prone. Our results indicate that employing either the drying soil–water retention curve or a mean soil–water retention curve (that attempts to average the wetting and drying retention curve) will underestimate the potential for failure of an unsaturated slope. It is suggested that when hysteresis cannot be considered, that the wetting soil–water retention curve be used for slope stability assessment. This approach would be consistent with the physical interpretation that an extreme rainfall event likely to trigger slope failure would follow the primary wetting soil–water retention curve. This study further illustrates the importance of including the dynamics of 3D unsaturated zone flow in simulating hydrologically driven slope failure.

Acknowledgments The study reported here was supported by National Science Foundation grant EAR-0409133. This effort would not have been possible without the site characterization and hydrologic observations completed by Bill Dietrich, Dave Montgomery, Ray Torres, Suzanne Anderson, Kevin Schmidt, and John Heffner.

References

Anderson MG, Howes S (1985) Development and application of a combined soil water—slope stability model. Q J Eng Geol Hydrogeol 18:225–236

Anderson MG, Kemp MJ, Lloyd DM (1988) Applications of soil water finite difference models to slope stability problems. In: Proceedings of the 5th international symposium on landslides. Lausanne, Switzerland, pp 525–550

Anderson SP (1995) Flow paths, solute sources, weathering, and denudation rates: The chemical geomorphology of a small catchment. PhD dissertation, University of California, Berkeley

Anderson SP, Dietrich WE (2001) Chemical weathering and runoff chemistry in a steep headwater catchment. Hydrol Process 15:1791–1815

Anderson SP, Dietrich WE, Montgomery DR, Torres R, Loague K (1997a) Concentration discharge relationships in runoff from a steep, unchanneled catchment. Water Resour Res 33:211–225

Anderson SP, Dietrich WE, Montgomery DR, Torres R, Conrad ME, Loague K (1997b) Subsurface flowpaths in a steep, unchanneled catchment. Water Resour Res 33:2637–2653

Anderson SP, Dietrich WE, Brimhall GH (2002) Weathering profiles, mass balance analysis, and rates of solute loss: linkages between weathering and erosion in a small, steep catchment. Geol Soc Am Bull 114:1143–1158

Andronopoulos B (1982) The geological structure and the tectonic evolution as factors of instability in the Pindos Zone area (Greece). Rock Mech 15:1–54

Bishop AW (1959) The principle of effective stress. Teknisk Ukeblad 39:859–863

Borja RI (2006) On the mechanical energy and effective stress in saturated and unsaturated porous continua. Int J Solids Struct 43:1764–1786

Cho SE, Lee SR (2002) Evaluation of surficial stability for homogeneous slopes considering rainfall characteristics. J Geotech Geoenviron 128:756–763

Chow VT (1959) Open-channel hydraulics. McGraw-Hill Book Company, New York, p 680

Christiansen JE (1942) Irrigation by sprinkling. California Agricultural Experiment Station Bulletin, Report 670

Duncan JM (1996) State of the art: limit equilibrium and finite-element analysis of slopes. J Geotech Eng ASCE 122:577–596

Dunne T (1990) Hydrology, mechanics, and geomorphic implications of erosion by subsurface flow. In: Higgins CG (ed) Groundwater geomorphology: the role of subsurface water in earth-surface processes and landforms, Special Paper, vol 252. Geological Society of America, Boulder, CO, pp 1–28

Dunne T (1994) Hydrogeomorphology—an introduction. Trans Jpn Geomorpholog Union 15A:1–4

Ebel BA, Loague K (2006) Physics-based hydrologic response simulation: Seeing through the fog of equifinality. Hydrol Process 20:2887–2900. doi:101002/hyp6388

Ebel BA, Loague K (2008) Rapid simulated hydrologic response within the variably saturated near surface. Hydrol Process 22:464–471. doi:101002/hyp6926

Ebel BA, Loague K, Dietrich WE, Montgomery DR, Torres R, Anderson SP, Giambelluca TW (2007a) Near-surface hydrologic response for a steep, unchanneled catchment near Coos Bay, Oregon: 1 Sprinkling experiments. Am J Sci 307:678–708. doi:102475/04200702

Ebel BA, Loague K, VanderKwaak JE, Dietrich WE, Montgomery DR, Torres R, Anderson SP (2007b) Near-surface hydrologic response for a steep, unchanneled catchment near Coos Bay, Oregon: 2 physics-based simulations. Am J Sci 307:709–748. doi:102475/04200703

Ebel BA, Loague K, Montgomery DR, Dietrich WE (2008) Physics-based continuous simulation of long-term near-surface hydrologic response for the Coos Bay experimental catchment. Water Resour Res 44:W07417. doi:101029/2007WR006442

Ebel BA, Mirus BB, Heppner CS, VanderKwaak JE, Loague K (2009) First-order exchange coefficient coupling for simulating surface water–groundwater interactions: parameter sensitivity and consistency with a physics-based approach. Hydrol Process 23:1949–1959. doi:101002/hyp7279

Evans SG (1982) Landslides and surficial deposits in urban areas of British Columbia; a review. Can Geotech J 19:269–288

Fourie AB, Rowe D, Blight GE (1999) The effect of infiltration on the stability of the slopes of a dry ash dump. Géotechnique 49:1–13

Freeze RA (1978) Mathematical models of hillslope hydrology. In: Kirkby MJ (ed) Hillslope hydrology. Wiley, New York, pp 177–225

Gasmo JM, Rahardjo HM, Leong EC (2000) Infiltration effects on stability of a residual soil slope. Comput Geotech 26:145–165

Godt JW, Baum RL, Lu N (2009) Landsliding in partially saturated materials. Geophys Res Lett 36:L02403

Gomi T, Sidle RC, Richardson JS (2002) Understanding processes and downstream linkages of headwater systems. Bioscience 52:905–916

Griffiths DV, Lane PA (1999) Slope stability analysis by finite elements. Geotechnique 49:387–403

Hattendorf I, St Hergarten, Neugebauer HJ (1999) Local slope stability analysis. In: St Hergarten, Neugebauer HJ (eds) Process modelling and landform evolution. Springer, New York, pp 169–185

Heppner CS, Loague K (2008) A dam problem: simulated upstream impacts for the Searsville Watershed. Ecohydrology 1:408–424

Heppner CS, Ran Q, VanderKwaak JE, Loague K (2006) Adding sediment transport to the Integrated Hydrology Model (InHM): development and testing. Adv Water Resour 9:930–943

Heppner CS, Loague K, VanderKwaak JE (2007) Long-term InHM simulations of hydrologic response and sediment transport for the R-5 catchment. Earth Surf Proc Land 32:1273–1292

Iverson RM (2000) Landslide triggering by rain infiltration. Water Resour Res 36:1897–1910

Johnson KA, Sitar N (1990) Hydrologic conditions leading to debris flow initiation. Can Geotech J 27:789–801

Jones JP, Sudicky EA, Brookfield AE, Park Y-J (2006) An assessment of the tracer-based approach to quantifying groundwater contributions to streamflow. Water Resour Res 42:W02407. doi:101029/2005WR004130

Kool JB, Parker JC (1987) Development and evaluation of closed-form expressions for hysteretic soil hydraulic properties. Water Resour Res 23:105–114

Krahn J, Lam L, Fredlund DG (1996) The use of finite element computed water pressures in slope stability analysis. In: Senneset K (ed) Proceedings of the seventh international symposium on landslides. Trondheim, Norway, pp 1277–1282

Lamberti GA, Gregory SV, Ashkenas LR, Wildman RC, Moore KM (1991) Stream ecosystem recovery following a catastrophic debris flow. Can J Fish Aquat Sci 48:196–208

Likos WJ, Lu N (2004) Hysteresis of capillary stress in unsaturated granular soil. J Eng Mech ASCE 130:646–655. doi:101061/ASCE073393992004130:6646

Loague K, VanderKwaak JE (2004) Physics-based hydrologic response simulation: Platinum bridge, 1958 Edsel, or useful tool. Hydrol Process 18:2949–2956

Loague K, Heppner CS, Abrams RH, VanderKwaak JE, Carr AE, Ebel BA (2005) Further testing of the Integrated Hydrology Model (InHM): event-based simulations for a small rangeland catchment located near Chickasha, Oklahoma. Hydrol Process 19:1373–1398

Loague K, Heppner CS, Mirus BB, Ebel BA, Ran Q, Carr AE, BeVille SH, VanderKwaak JE (2006) Physics-based hydrologic-response simulation: foundation for hydroecology and hydrogeomorphology. Hydrol Process 20:1231–1237

Lu N, Godt J (2008) Infinite slope stability under steady unsaturated seepage conditions. Water Resour Res 44:W11404

Lu N, Likos WJ (2006) Suction stress characteristic curve for unsaturated soil. J Geotech Geoenviron 132:131–142

Mirus BB, Ebel BA, Loague K, Wemple BC (2007) Simulated effect of a forest road on near surface hydrologic response. Redux Earth Surf Proc Land 32:126–142. doi:101002/esp1387

Mirus BB, Loague K, VanderKwaak JE, Kampf SK, Burges SJ (2009) A hypothetical reality of Tarrawarra-like hydrologic response. Hydrol Process 23. doi:101002/hyp7241

Montgomery DR, Dietrich WE (2002) Runoff generation in a steep, soil-mantled landscape. Water Resour Res 38:1168–1175

Montgomery DR, Dietrich WE, Torres R, Anderson SP, Heffner JT, Loague K (1997) Hydrologic response of a steep, unchanneled valley to natural and applied rainfall. Water Resour Res 33:91–109

Montgomery DR, Dietrich WE, Heffner JT (2002) Piezometric response in shallow bedrock at CB1: implication for runoff generation and landsliding. Water Resour Res 38:1274–1292

Montgomery DR, Schmidt KM, Dietrich WE, McKean J (2009) Instrumental record of debris flow initiation during natural

rainfall: implications for modeling slope stability. J Geophys Res 114:F01031. doi:10.1029/2008JF001078
Ng CWW, Shi Q (1998a) Influence of rainfall intensity and duration on slope stability in unsaturated soils. Q J Eng Geol 31:105–113
Ng CWW, Shi Q (1998b) A numerical investigation of the stability of unsaturated soil slopes subjected to transient seepage. Comput Geotech 22:1–28
Rahardjo H, Lim TT, Chang MF, Fredlund DG (1994) Shear strength characteristics of a residual soil. Can Geotech J 32:60–77
Ran Q, Heppner CH, VanderKwaak JE, Loague K (2007) Further testing of the Integrated Hydrology Model (InHM): multiple-species sediment transport. Hydrol Process 21:1522–1531
Roering JJ, Schmidt KM, Stock JD, Dietrich WE, Montgomery DR (2003) Shallow landsliding, root reinforcement, and the spatial distribution of trees in the Oregon Coast Range. Can Geotech J 40:237–253
Roering JJ, Kirchner JW, Dietrich WE (2005) Characterizing structural and lithologic controls on deep-seated landsliding; implications for topographic relief and landscape evolution in the Oregon Coast Range, USA. Geol Soc Am Bull 117:654–668
Scheidegger AE (1972) Hydrogeomorphology. J Hydrol 20:193–215
Schmidt KM (1999) Root strength, colluvial soil depth, and colluvial transport on landslide-prone hillslopes. PhD Dissertation, Department of Geological Sciences, University of Washington, Seattle
Schmidt KM, Roering JJ, Stock JD, Dietrich WE, Montgomery DR, Schaub T (2001) The variability of root cohesion as an influence on shallow landslide susceptibility in the Oregon Coast Range. Can Geotech J 38:995–1024
Schrefler BA (1984) The finite element method in soil consolidation (with applications to surface subsidence). PhD dissertation, University College of Swansea, Swansea, UK
Scott PS, Farquhar GJ, Kouwen N (1983) Hysteretic effects on net infiltration. In: Advances in infiltration, Publication 11–83. American Society of Agricultural Engineers, St. Joseph, pp 163–170
Sidle RC, Ochiai H (2006) Landslides: processes, prediction and land use. Water Resources Monograph 18. American Geophysical Union, Washington, p 312
Sidle RC, Onda Y (2004) Hydrogeomorphology: overview of an emerging science. Hydrol Process 18:597–602. doi:101002/hyp1360
Simoni S, Zanotti F, Bertoldi G, Rigon R (2008) Modelling the probability of occurrence of shallow landslides and channelized debris flows using GEOtop-FS. Hydrol Process 22:532–545
Smerdon BD, Medoza CA, Devito KJ (2007) Simulations of fully coupled lake groundwater exchange in a subhumid climate with an integrated hydrologic model. Water Resour Res 43:W01416. doi:101029/2006WR005137
Stark TD, Eid HT (1998) Performance of three-dimensional slope stability methods in practice. J Geotech Geoenviron 124:1049–1060
US Geological Survey (2004) Landslide types and processes fact sheet 2004-3072
Taylor G, Hale C, Joos S (2005) Climate of Coos County. Special report, Oregon Climate Service, Corvallis, Oregon, Oregon State University, pp 1–4
Terzaghi K (1943) Theoretical soil mechanics. Wiley, New York
Torres R (1997) Unsaturated zone processes and the hydrologic response of a steep, unchanneled valley. PhD Dissertation, University of California, Berkeley
Torres R, Dietrich WE, Montgomery DR, Anderson SP, Loague K (1998) Unsaturated zone processes and the hydrologic response of a steep, unchanneled catchment. Water Resour Res 34:1865–1879
Tsaparas I, Rahardjo H, Toll DG, Leung EC (2002) Controlling parameters for rainfall-induced landslides. Comput Geotech 29:1–27
Van Asch ThWJ, Buma J, Van Beek LPH (1999) A view on some hydrological triggering systems in landslides. Geomorphology 30:25–32
van Genuchten MTh (1980) A closed-form equation for predicting the hydraulic conductivity of unsaturated soils. Soil Sci Soc Am J 44:892–898
VanderKwaak JE (1999) Numerical simulation of flow and chemical transport in integrated surface-subsurface hydrologic systems. PhD dissertation, University of Waterloo, Ontario, Canada
VanderKwaak JE, Loague K (2001) Hydrologic-response simulations for the R-5 catchment with a comprehensive physics-based model. Water Resour Res 37:999–1013
Vieira BC, Fernandes NF (2004) Landslides in Rio de Janeiro: the role played by variations in soil hydraulic conductivity. Hydrol Process 18:791–805
Wilkinson PL, Anderson MG, Lloyd DM (2002) An integrated hydrological model for rain-induced landslide prediction. Earth Surf Proc Land 27:1285–1297
Wilson CJ, Dietrich, WE (1987) The contribution of bedrock groundwater flow to storm runoff and high pore pressure development in hollows. In: Beschta RL, Blinn T, Grant GE, Ice GG, Swanson FJ (eds) Proceedings of the international symposium on erosion and sedimentation in the Pacific Rim, IAHS Publication 165, pp 49–59
Wong F (1984) Uncertainties in FE modeling of slope stability. Comput Struct 19:777–791
Wright SG, Kulhawy FG, Duncan JM (1973) Accuracy of equilibrium slope stability analysis. J Soil Mech Found Div ASCE 99:783–791
Wu Y-S, Haukwa C, Bodvarsson GS (1999) A site-scale model for fluid and heat flow in the unsaturated zone of Yucca Mountain. J Contam Hydrol 38:185–215